



# Structural and Optical Properties of Nanocrystalline 3-(2-Benzothiazolyl)-7-(diethylamino) Coumarin (C6) Thin Films for Optoelectronic Application

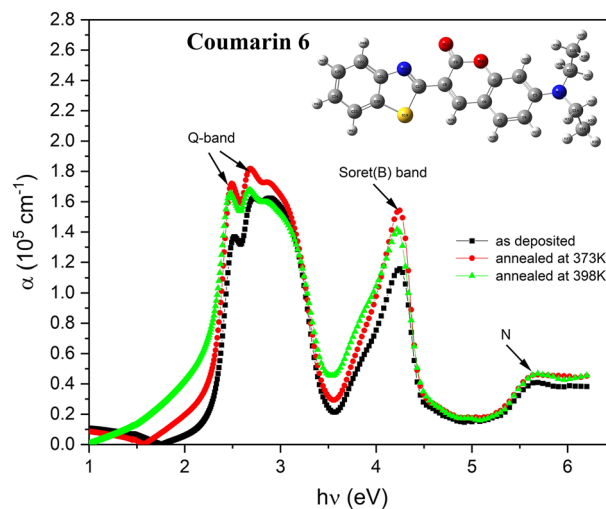
Mostafa Saad Ebied<sup>1</sup> · Mahmoud Dongol<sup>1</sup> · Medhat Ibrahim<sup>2,3</sup> · Mohammed Nassary<sup>4</sup> · Sahar Elnobi<sup>4</sup> · Amr Attia Abuelwafa<sup>1</sup>

Received: 21 February 2022 / Accepted: 22 June 2022 / Published online: 18 July 2022  
© The Author(s) 2022

## Abstract

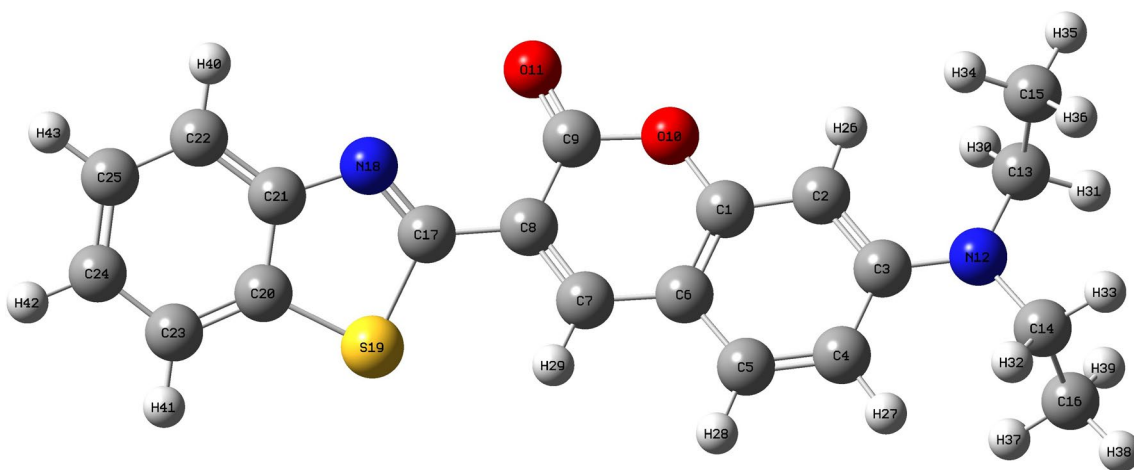
In the current work, the structural and optical properties of thermally evaporated 3-(2-Benzothiazolyl)-7-(diethylamino) coumarin [Coumarin 6 (C6)] thin films on a pre-cleaned quartz substrate were studied as a function of the annealing temperature. The influence of annealing on the structural, morphological, and molecular structures was investigated by x-ray diffraction (XRD), atomic force microscopy (AFM), and Fourier transform infrared (FTIR) spectroscopy, respectively. The XRD and AFM results confirmed that the as-deposited and annealed films have nanostructural features (30.96–45.34 nm). Also, the increase in roughness of the C6 thin film surface resulted from particle agglomeration and coalescence. Optical constants of C6 thin films were derived from the transmittance  $T(\lambda)$  and reflectance,  $R(\lambda)$  measurements in the spectral range of 200–2500 nm. Analysis of the optical absorption coefficient data indicates that the type of electronic transition in these films is an indirect allowed transition. The estimated optical band gap was decreased from 2.12 eV to 2.01 eV as the annealing temperature was increased. Dispersion and dielectric parameters were determined as functions of the annealing temperature. Lastly, nonlinear optical parameters such as the third-order nonlinear susceptibility,  $\chi^{(3)}$  and nonlinear refractive index,  $n_{(2)}$  were estimated and influenced by annealing temperature. The optical properties of C6 thin films were showed that C6 thin films would be used in a wide range of photonic applications

## Graphical Abstract



**Keywords** Coumarin 6 (C6) · thin films · thermal annealing · optical properties · nonlinear optical properties

Extended author information available on the last page of the article



**Scheme 1** Molecular structure of C6 Dye.

## Introduction

The performance of organic-based microelectronic devices is affected by the characteristics of the organic molecules utilised in their fabrication, as well as their optical and electrical properties.<sup>1</sup> Thus, organic materials have risen in popularity because of their numerous applications in photonic devices such as organic light-emitting diodes (OLEDs), organic photovoltaics (OPVs), and organic solid-state lasers.<sup>2–5</sup> Coumarin and its derivatives have received a considerable interest in industry in the form of dye lasers and high-efficiency dye-sensitized solar cells due to their interesting and promising optical features, such as fluorescence in visible light, significant Stokes shifts, high quantum yields, and solubility.<sup>6</sup> Recently, a few studies have focused on the relationship between the molecular structure and optical properties of coumarin to gain better knowledge of the electronic operational principles, which may result in more efficient coumarin derivatives for optical device applications.<sup>7,8</sup> Coumarin 6 (C6), a chromophore of the highly conjugated coplanar molecule, has been identified and employed as a fluorescent dye for staining organelles or medical materials<sup>9,10</sup> and as a high-gain medium in tunable and amplifier lasers.<sup>11,12</sup> C6 has generated substantial attention in optoelectronic applications after its successful introduction as an effective dopant in organic light-emitting diodes (OLEDs).<sup>13,14</sup> Such as OLEDs with low turn-on voltages were fabricated in polyvinylcarbazol (PVK) doped with C6 deposited using ink-jet printing<sup>15</sup> and spin coating.<sup>16</sup> Also, Ismail et al. used C6 dye was used as a donor material in bulk heterojunctions (BHJ),<sup>17</sup> and they studied the effect of the dye on light harvesting and photocurrent of the P3HT:PCBM solar cell.<sup>18</sup> The performance of N719

sensitized nanocrystalline TiO<sub>2</sub> DSSC<sup>19</sup> was examined by adding C6 to the electrolyte, which improves not only the short-circuit current but also the fill factor and device efficiency.

Recently, our group performed DFT and TDDFT calculations<sup>20</sup> to investigate the effect of attaching two different acceptor groups (–COOH and –CN) to C6 dye on the electronic structure and optical properties of the novel dyes and the use of these dyes as sensitizers for DSSCs. A thorough investigation of the fabrication and characterization of Coumarin 6 polycrystalline or amorphous thin films for use in organic multilayer optoelectronic devices is required. To achieve this goal, C6 thin films were obtained using the technique of thermal evaporation in this study, and their structure was investigated in terms of X-ray diffraction and FTIR spectroscopy, whereas the optical properties such as refractive index *n* and optical band gap energy were derived from the measurements of the transmittance and reflectance. Using a single oscillator model, the dispersion of the refractive index was explored and analyzed. In addition, we computed the nonlinear optical parameters  $\chi^{(3)}$  and  $n_{(2)}$ . We also examined the effect of annealing on the structural and optical properties of as-deposited C6 thin films.

## Experimental Technique

C6 (Scheme 1) was obtained from Sigma-Aldrich, and C6 thin films were deposited onto clean quartz surfaces for optical and structural studies using Edward's coating unit (E 306A). A quartz crystal monitor, FTM5, was used to regulate the evaporation rate (0.3 nm/s) and the thickness of the evaporated films (260 nm). A group of these films was annealed in air at 373 and 398 K for 2 h before progressively cooling to room temperature. X-ray diffraction

patterns for C6 as-deposited and annealed thin films were obtained using an XRD system equipped with a Rigaku RINT 2100 diffractometer. Chemical structural characterizations of the powder, as-deposited, and annealed thin films were performed at room temperature using FTIR spectroscopy (Jasco Model 6100) with a resolution of  $1\text{ cm}^{-1}$  in the spectral range  $400\text{--}4000\text{ cm}^{-1}$ . Surface characterization of the prepared C6 thin films was examined by AFM (NT-MDT, Russia). The transmittance  $T(\lambda)$  and reflectance  $R(\lambda)$  measurements were carried out at normal incidence at room temperature in a wide wavelength range between 200 and 2500 nm using a double-beam JASCO-670 UV computer-controlled spectrophotometer for all the investigated films.

The optical constants of the studied thin films such as the absorption coefficient,  $\alpha$ , absorption index,  $k$ , and the refractive index,  $n$ , at different wavelengths,  $\lambda$ , were computed using the following equations<sup>21–23</sup>:

$$\alpha = \frac{1}{d} \ln \left[ \frac{(1-R)^2}{2T} + \sqrt{\frac{(1-R)^4}{4T^2} + R^2} \right] \quad (1)$$

$$k = \frac{\alpha \lambda}{4\pi} \quad (2)$$

$$n = \frac{1+R}{1-R} + \sqrt{\frac{4R}{(1-R)^2} - k^2} \quad (3)$$

where  $d$  is the film thickness with experimental errors  $\pm 2.5\%$ .

## Results and Discussion

### Structural Properties

C6 in powder form exhibits an XRD pattern, which is seen in Fig. 1a. It is clear from the pattern that the C6 powder is polycrystalline, as shown by the presence of several diffraction peaks of various intensities. C6 has a triclinic structure (CCDC reference:1294096) with space group  $P\bar{1}$  and lattice parameters  $a = 8.962\text{ \AA}$ ,  $b = 11.136\text{ \AA}$ ,  $c = 8.922\text{ \AA}$ ,  $\alpha = 95.14^\circ$ ,  $\beta = 104.50^\circ$ , and  $\gamma = 86.74^\circ$ .<sup>1,24,25</sup> The XRD patterns of the investigated thin films are presented in Fig. 1b, indicating that the as-deposited and annealed C6 thin films are partially crystallized. The intensity of the prominent peak at  $2\theta = 13.7^\circ$  increases when the annealing temperature is raised. This result might be explained by rearrangements in the film atomic structure, which boosts their crystallinity.<sup>26</sup> The average crystallite size  $D$  was estimated using Scherrer's equation<sup>27,28</sup>

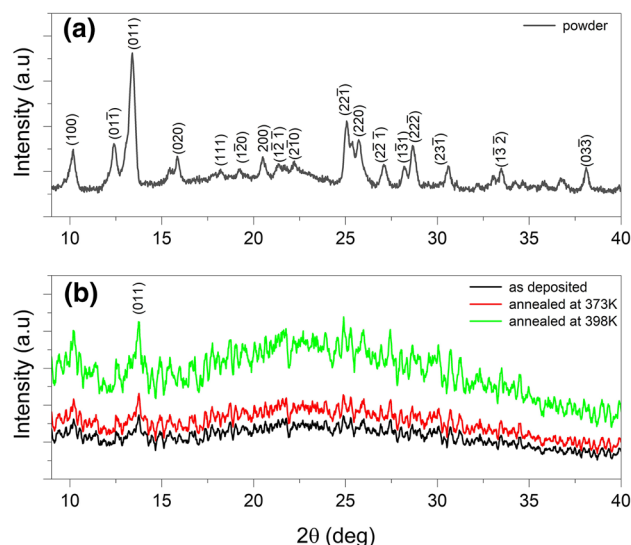


Fig. 1 XRD pattern of (a) powder and (b) the investigated thin films.

$$D = \frac{K_S \lambda}{\beta \cos \theta} \quad (4)$$

where  $\theta$  is Bragg's angle,  $\beta$  is the FWHM in radians,  $\lambda = 0.15406\text{ nm}$  for an X-ray wavelength of  $\text{CuK}\alpha$ , and  $K_S = 0.94$  is a constant known as the shape factor. Crystallite sizes estimated using Scherrer's equation are listed in Table 1. Crystallite size values are in the nanoscale, confirming the nanostructural properties of the as-deposited and annealed films. In addition, the nano-size nature of the as-deposited and annealed thin films is represented in the broadening or FWHM of the (011) plane diffraction peak in the thin film pattern, which is bigger than that of the source powder of C6. The broadening of the (011) plane's diffraction peak may be attributed to tiny crystallites, which result in significant surface scattering and hence cause a significant broadening of the diffraction peak. During film deposition and post-annealing, it is possible for some strain and dislocation to occur in the film. The dislocation density,  $\delta$ , has been estimated using Williamson and Smallman's formula<sup>29</sup> as the length of dislocation lines per unit volume of the crystal using crystallite size values ( $D$ ).

$$\delta = \frac{1}{D^2} \quad (5)$$

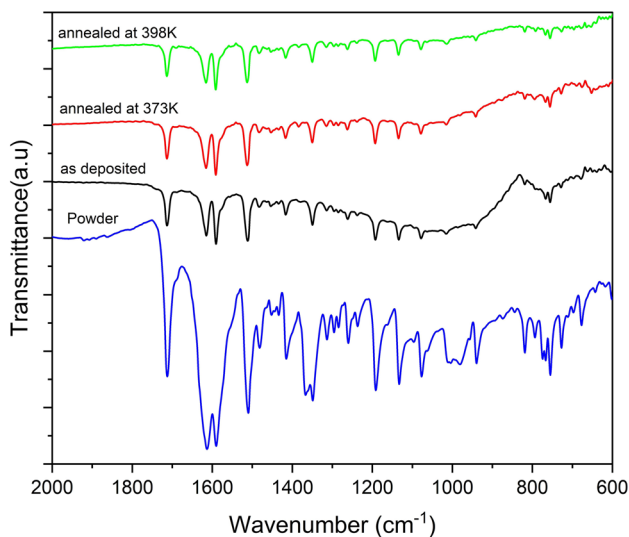
The microstrain,  $\epsilon_s$ , derived from the following equation<sup>27</sup>:

$$\epsilon_s = \frac{\beta \cos \theta}{4} \quad (6)$$

The number of crystallites per unit surface area,  $N_c$ , can be calculated using the following formula<sup>27,28,30</sup>:

**Table I** Structural parameters for C6 powder, as-deposited and annealed thin films

C6 thin film condition	D (nm)±0.02	$\delta$ (lin m) <sup>-2</sup> ×10 <sup>15</sup> ±0.02	$\epsilon$ ×10 <sup>-3</sup> ±0.02	$N_c$ (m <sup>-2</sup> )×10 <sup>16</sup> ±0.02
Powder	23.04	1.88	1.57	1.226
As-deposited	30.96	1.043	1.17	0.505
Annealed at 373 K	36.71	0.742	0.986	0.303
Annealed at 398 K	45.34	0.486	0.798	0.161

**Fig. 2** FTIR spectra of powder and the investigated thin films.

$$N_c = \frac{d}{D^3} \quad (7)$$

The values of  $\delta$ ,  $\epsilon_s$ , and  $N_c$  at different annealing temperatures are given in Table I. As seen in the table, the microstrain, dislocation density, and a number of crystallites all decrease with increasing annealing temperature, while the crystallite size increases. The decrease in the concentration of lattice flaws (point defects) near the grain boundary areas causes this phenomenon. At higher annealing temperatures, the development of high-quality C6 thin films is demonstrated by lower microstrain and dislocation density. The increased diffusion of species and the formation of films with bigger crystallites were aided by the thermal energy complete by annealing.

The infrared spectrum is a widely used and successful method for determining the molecular structure of a wide variety of materials, both organic and inorganic. The infrared spectra of the C6 powder and thin films in various forms are shown in Fig. 2 in the spectra range 600–2000  $\text{cm}^{-1}$ . Table II includes the peak's locations and assignments, which match the C6 powder spectra's stated places. Because C6 molecules do not disintegrate during the thermal evaporation process and C6 films have excellent chemical stability and stoichiometric films, this indicates that C6 is a good choice for thermal deposition. AFM is used to analyze and evaluate

the surface morphology, roughness, and grain size of the thin film before and after annealing. Figure 3 illustrates the changes in the microstructure before and after different annealing treatments. It is plain to observe that the form of the grains varies throughout the annealing process and that the grain boundaries fade as the grains merge. The as-deposited thin film has a root-mean-square (RMS) roughness of  $2.618 \pm 0.03$  nm while the RMS value for the annealed thin film is  $7.385 \pm 0.03$  nm. The increase in the roughness of the C6 thin film surface is a result of particle agglomeration and coalescence. As predicted, the surface morphology of the films varies with increasing the annealing temperature. This is consistent with the XRD and demonstrates that increasing the annealing temperature modifies the thin film structure.

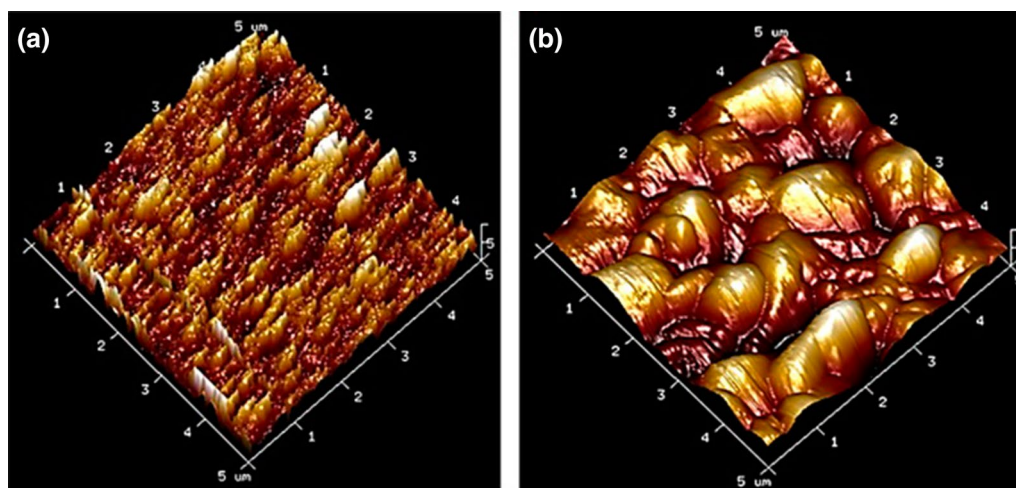
## Optical Properties

The  $T(\lambda)$  and  $R(\lambda)$  spectra of as-deposited and annealed thin films in the wavelength range 200–2500 nm are shown in Fig. 4. All films become almost transparent in the non-absorbing zone (i.e.,  $R + T = 1$ ) at longer wavelengths ( $\lambda > 750$  nm) owing to the negligible energy loss due to scattering. Absorption occurs because of the inequality ( $A + R + T = 1$ ) at lower wavelengths ( $\lambda < 750$  nm), which is referred to as the absorbing area. In addition, the annealing temperature pushes the transmittance edge to higher wavelengths, making it easier to see through the material. Because light scattering occurs on rough surfaces, it is often considered that the transmittance of a film decreases with grain size in the visible light range.<sup>31,32</sup> As a result, the annealing is expected to have an impact on the gap. Increasing the annealing temperature of C6 thin films decreases the optical reflectance of the as-deposited film, as shown in Fig. 4.

Figure 5 illustrates the absorption coefficient of the as-deposited and annealed C6 thin films, which has a value in the range of  $10^5 \text{ cm}^{-1}$ . Three bands are seen in these spectra. The Q band is associated with a transition from the ground state to the first excited state ( $S_0 \rightarrow S_1$ ), while the Soret (B) band corresponds to a strongly allowed transition from the ground state to the second excited state ( $S_0 \rightarrow S_2$ ). The Q and Soret (B) bands are often assigned to  $\pi \rightarrow \pi^*$  singlet transitions.<sup>33</sup> A band designated N appears in the ultraviolet region at 225 nm due to the intrinsic transition of C6 ( $n \rightarrow \pi^*$ ).<sup>28</sup> Using Tauc's relation, which

**Table II** Peak positions and assignments for C6 powder, as-deposited and annealed thin films

	Powder	As-deposited	Annealed at 398 K	Annealed at 398 K
C=O stretching (1670–1820) $\text{cm}^{-1}$	1712	1713	1714	1714
C=C stretching (1550–1615) $\text{cm}^{-1}$	1615	1615	1616	1616
C=N Stretching	1590	1590	1590	1591
C-C Stretching	1509	1512	1512	1512
C-N Stretching	1348	1349	1350	1350
C-H in-plane bending (1225–950) $\text{cm}^{-1}$	1191	1192	1193	1192
	1132	1133	1134	1134
	1077	1078	1078	1078
C-H out-of-plane bending (900–670) $\text{cm}^{-1}$	939	942	942	942
	818	819	818	819
	754	754	755	755
	727	728	727	727
	676	678	675	678
C-S Stretching	676	678	675	678

**Fig. 3** AFM images for (a) as-deposited and (b) annealed thin films.

describes the interband absorption coefficient as a function of energy in the region of the absorption edge, it is usual to investigate both the types of optical transitions and the magnitude of the energy gap at the basic absorption edge in numerous organic thin films<sup>34</sup>:

$$\alpha h\nu = A(h\nu - E_g)^r \quad (8)$$

where  $h\nu$  is the photon energy,  $A$  is a constant called the band tailing,  $E_g$  is the energy of the optical band gap, and  $r$  determines the type of the optical transition, when  $r = 2$ , the best fit of the experimental data to Eq. 8 is achieved. This means that the electronic transition is an indirect allowed transition, as seen in Fig. 6 by plotting  $(\alpha h\nu)^{1/2}$  versus  $h\nu$  for the as-deposited and annealed films. Values of optical energy gap for each electronic transition are obtained by extrapolating

the straight lines parts of the curves to  $(\alpha h\nu)^{1/2} = 0$  and are tabulated in Table III. The optical energy gaps  $E_g^Q$ ,  $E_g^B$  and  $E_g^N$  correspond to the optical absorption in the Q band, Soret (B) and N energy bands, respectively. The calculated energy gap for Q band  $E_g^Q$  between HOMO and LUMO orbitals of as-deposited C6 film is in good agreement with the reported values.<sup>35</sup> The reduction in the energy gap values (e.g., a red-shift) with higher annealing temperatures is attributed to an increase in crystallite size as well as a decrease in lattice defect concentration at the grain boundary.<sup>36,37</sup> Additionally, a shift in the relative locations of the valence (HOMO;  $\pi$  orbitals) and conduction band (LUMO;  $\pi^*$  orbitals) might minimize the energy gap, which occurs from the thermal energy generated during annealing.<sup>37,38</sup> The behaviour of the energy gap values in C6 films as a function of annealing

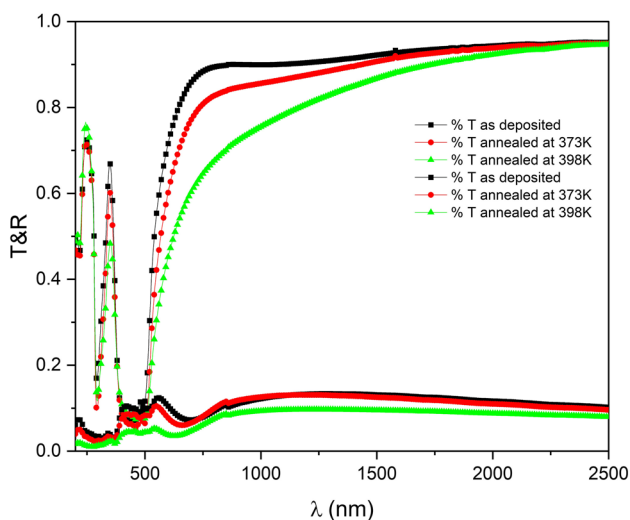


**Fig. 4** The optical transmission  $T(\lambda)$  and reflection  $R(\lambda)$  for as-deposited and annealed thin films.

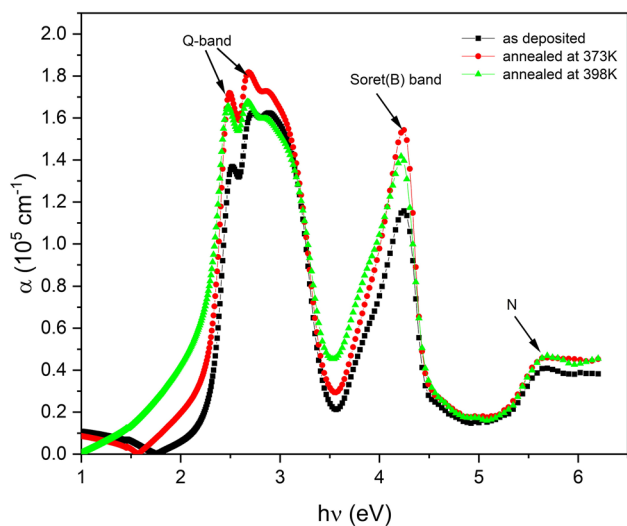


**Fig. 5** Absorption coefficient,  $\alpha$  for as-deposited and annealed thin films as a function of  $h\nu$ .

temperature appears to be comparable to that observed in previously reported organic films.<sup>36–40</sup>

**Dispersion Analysis of the Refractive Index n**

The complex refractive index  $N = n - jk$  of electromagnetic waves travelling through thin films is frequency-dependent, while the refractive index  $n$  which is the real part of the complex refractive index is velocity-dependent and carries information about electronic polarisation.<sup>37,41</sup> The imaginary component (extinction coefficient,  $k$ ) is proportional to the decay or damping of the applied

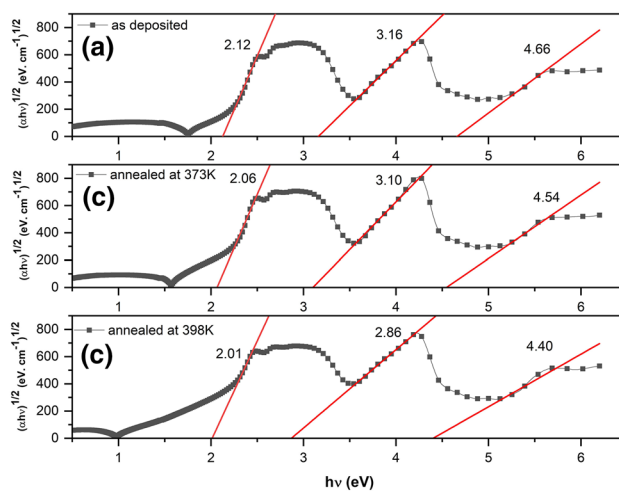


**Fig. 6**  $(ah\nu)^{1/2}$  versus  $h\nu$  for C6 thin films (a) as-deposited, (b) annealed at 373 K and (c) annealed at 398 K.

**Table III** Variation of the optical band gap of C6 thin films for different annealing temperatures.

C6 thin film condition	$E_g^Q \pm 0.01$	$E_g^B \pm 0.01$	$E_g^N \pm 0.01$
As-deposited	2.12	3.16	4.66
Annealed at 373 k	2.06	3.10	4.54
Annealed at 398 k	2.01	2.86	4.4

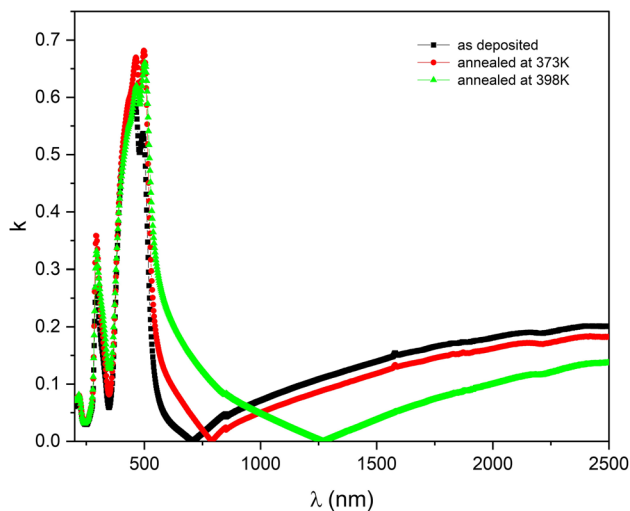


**Fig. 7** Extinction coefficient,  $k$  for as-deposited and annealed thin films as a function of wavelength.

electric field's oscillation amplitude. The spectra of the  $k(\lambda)$  curves for the investigated thin films are presented in Fig. 7. As shown in Fig 7, the  $k$  for as-deposited and annealed C6 thin films approach a minimum value at about 900 nm. After that,  $k$  increases again with an increasing

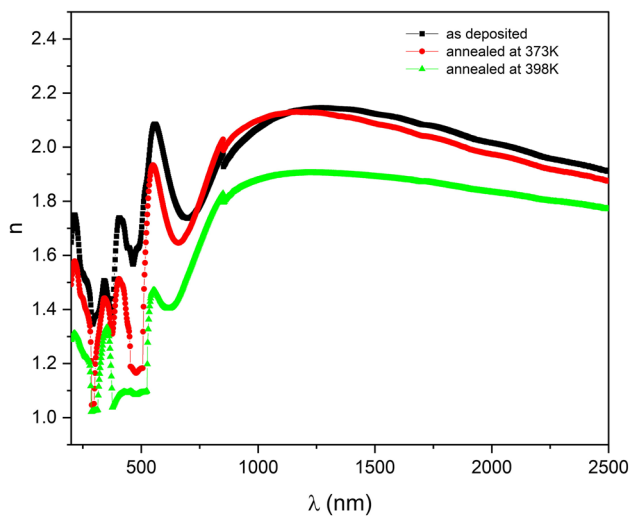


**Fig. 8** Reflective index,  $n$  for as-deposited and annealed thin films as a function of wavelength.

wavelength, which is a characteristic feature of the presence of free carriers in C6 film.<sup>42–44</sup> When the annealing temperature was raised, the peak locations changed slightly toward a longer wavelength (redshift) and their intensity increased. This behavior may be explained by the fact that the crystallite size grows as the annealing temperature increases. Figure 8 represents the change in  $n$  as a function of  $\lambda$  for as-deposited and annealed C6 films. It is found that annealing changes the locations of the peaks a lot, which is related to changes in the structures of the thin films. The fluctuation of the refractive index  $n$  with wavelength (dispersion of  $n$ ) is also a critical optical property of thin film materials used to transmit electromagnetic waves.<sup>43</sup> The dispersion curve was analysed using the two-zone method (see Fig. 8). Numerous peaks in the refractive index are seen in the first region at  $\lambda < 750$  nm. When absorption occurs inside this zone,  $n$  reverts to its original orientation when absorption decreases to the non-absorbing region (second region)  $\lambda > 750$  nm.<sup>37</sup> Additionally,  $n$  drops gradually as  $\lambda$  increases in this area. This is known as normal dispersion.<sup>37</sup> The normal dispersion behavior is caused by the effect of the resonance between the incident electromagnetic radiation and the electron's polarization, which couples electrons in C6 films to the oscillating electric field. The  $n$  in the second region can be analyzed using the single-oscillator model suggested by Wemple-DiDomenico (WDD) using the following equation<sup>45</sup>:

$$n^2 = 1 + \frac{E_d E_o}{E_o^2 - (h\nu)^2} \quad (9)$$

where  $E_o$  and  $E_d$  are the single-oscillator energy and oscillator dispersion energy, respectively.  $E_d$  indicates the average

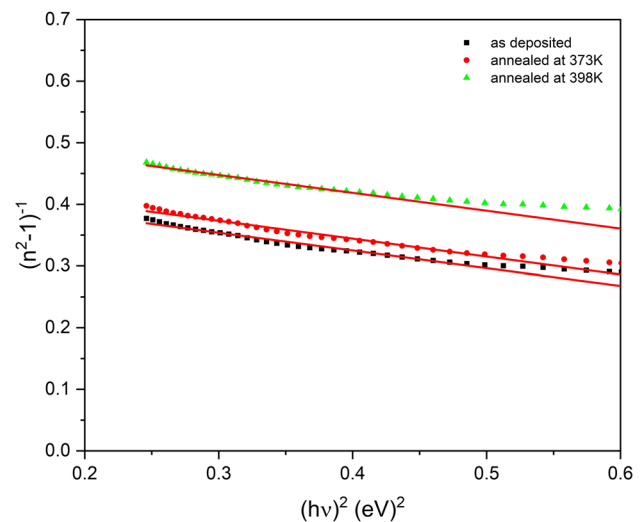


**Fig. 9**  $(n^2 - 1)^{-1}$  versus  $(h\nu)^2$  for as-deposited and annealed thin films.

strength of interband optical transitions and is connected to variations in the structural order of the material; nevertheless, the  $E_o$  is considered the material's average energy gap value. The  $E_d$  and  $E_o$  values can be easily obtained from the slope  $(E_o E_d)^{-1}$  and the intercept  $(E_o/E_d)$  by plotting of  $(n^2 - 1)^{-1}$  versus  $(h\nu)^2$  for as-deposited and annealed films as illustrated in Fig. 9. The obtained values of  $E_d$  and  $E_o$  are given in Table IV. As the annealing temperature increases, the values of  $E_d$  are decreased while the values of  $E_o$  are increased. Extrapolating the linear part of the dispersion relationship towards  $h\nu = 0$  gives the infinite wavelength dielectric constant  $\epsilon_\infty$ . Also, the static refractive index  $n_o$ , can be used to calculate using the formula ( $n_o = \sqrt{\epsilon_\infty}$ ). The values of  $\epsilon_\infty$  and  $n_o$  C6 thin films are tabulated in Table IV.

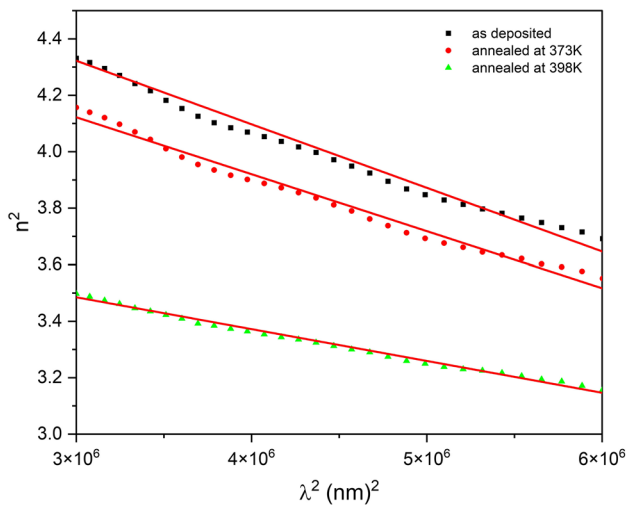
The dielectric constant at high frequency  $\epsilon_L$  can be calculated by analyzing the refractive index  $n$  data as follows. In the transparent region, the relation between the refractive index,  $n$ , the high frequency dielectric constant,  $\epsilon_L$ , and the wavelength  $\lambda$ , is given by the relation<sup>46,47</sup>:

$$n^2 = \epsilon_L - \left( \frac{e^2}{4\pi^2 c^2 \epsilon_o} \right) \left( \frac{N}{m^*} \right) \lambda^2 \quad (10)$$

where  $e$  is the electronic charge,  $\epsilon_o$  is the vacuum permittivity  $N/m^*$  is the ratio of charge carrier concentration to the effective mass of the charge carriers. The variation of  $n^2$  vs.  $\lambda^2$  for C6 films is shown in Fig. 10. At longer values of wavelengths the dependence of  $n^2$  on  $\lambda^2$  is linear, which can be extrapolated to zero wavelength ( $\lambda^2 = 0$ ) to calculate the high-frequency dielectric constant  $\epsilon_L$  and the slope of this linear part can be used to evaluate the value of  $N/m^*$ . The plasma frequency  $\omega_p$  can be calculated as following based on the Drude model<sup>40,48</sup>:

**Table IV** Optical parameters of C6 thin films for different annealing temperatures

C6 thin film condition	$n_{0\pm 0.01}$	$\epsilon_{\infty\pm 0.01}$	$E_o \pm 0.01$	$E_d \pm 0.01$	$N/m^*$ ( $m^{-3}Kg^{-1}$ ) $\times 10^{56}$ $\pm 0.02$	$\epsilon_{L\pm 0.02}$	$\omega_p^2$ ( $Hz$ ) $\times 10^{30} \pm 0.02$	$\chi^{(3)} \times 10^{-13}$ esu $\pm 0.02$	$n_2 \times 10^{-12}$ esu $\pm 0.02$
As-deposited	1.82	3.33	4.19	9.56	2.74	4.99	1.12	2.02	4.17
Annealed at 373 k	1.79	3.21	4.26	9.05	2.64	4.72	1.07	1.61	3.39
Annealed at 398 k	1.71	2.93	4.65	8.96	1.22	3.82	0.51	0.94	2.07

**Fig. 10**  $n^2$  versus  $\lambda^2$  for as-deposited and annealed thin films.

$$\omega_p^2 = \frac{e^2 N / m^*}{\epsilon_o} \quad (11)$$

The values of these parameters are listed in Table IV. It is obvious that the value of  $\epsilon_{\infty} < \epsilon_L$ , may be attributed to the contribution of free charge carriers to the polarisation process occurring within the material when light illuminates it.<sup>37</sup> Moreover, the decreasing values of  $\epsilon_{\infty}$  and  $\epsilon_L$  with the annealing temperature increases may be ascribed to the reduction of lattice vibration and bound carriers in the transparent zone.

### Dielectric Characterization

The dielectric constant  $\epsilon^*$  is a critical element in the manufacture and design of highly efficient optical-electronic systems. The complex dielectric function is written as  $\epsilon^*(\omega) = \epsilon_1(\omega) + \epsilon_2(\omega)$  with the real  $\epsilon_1$  and imaginary  $\epsilon_2$  parts of components. The optical constant components can be derived from  $n$  and  $k$  using the following formulas<sup>22,28</sup>:

$$\epsilon_1(\omega) = n^2 - K^2 \text{ and } \epsilon_2(\omega) = 2nK \quad (12)$$

The  $\epsilon_1$  and  $\epsilon_2$  components of the dielectric constant are shown as a function of the photon energy  $h\nu$  of the investigated C6 thin film in Fig. 11. Through the interaction of incoming photons and electrons, the presence of peaks in the dielectric spectrum identifies the type of material and offers information on the electronic structure of the material. As seen in Fig. 11, increasing the annealing temperature of C6 thin films resulted in a decrease in the  $\epsilon_1$  and  $\epsilon_2$ . The decrease in the dielectric constants of C6 thin films as annealing temperatures increase might be a result of a decrease in net polarisation produced by a decrease in the net alignment of dipoles within materials generated by the electric field during thermal annealing.<sup>49-52</sup> The dissipation factor (loss tangent,  $\tan \delta$ ) is a property of dielectric materials that measure their intrinsic energy dissipation due to the molecule's inability to realign them in response to an applied alternating electric field and may be estimated using the following equation<sup>21,22</sup>:

$$\tan \delta = \frac{\epsilon_2}{\epsilon_1} \quad (13)$$

The plot of  $\tan \delta$  vs.  $h\nu$  for the investigated C6 thin films is shown in Fig. 12. The peaks in the spectra represent the mean energy dissipation of C6 thin films owing to interband transitions. As the temperature increases,  $\tan \delta$  switches to a higher frequency, suggesting a thermally triggered process.<sup>52,53</sup> The volume energy loss function (VELF) and surface energy loss function (SEF) are two well-known variables that measure the rate at which high-energy electrons lose energy while traveling through the medium (SELF). The following relationship<sup>22</sup> connects VELF and SELF to the real and imaginary terms of a dielectric function:

$$\text{VELF} = -\text{Im}\left(\frac{1}{\epsilon^*}\right) = \frac{\epsilon_2}{\epsilon_1^2 + \epsilon_2^2} \quad (14)$$



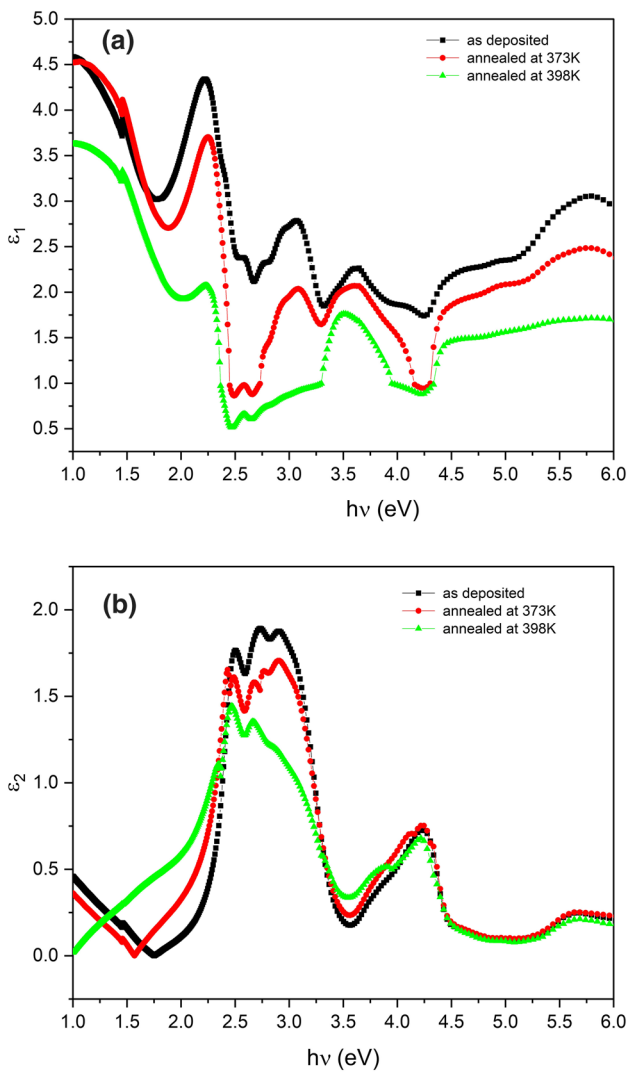


Fig. 11 The variation of (a) the  $\epsilon_1$  and (b) the  $\epsilon_2$  part with  $h\nu$  for as-deposited and annealed thin films.

$$SELF = -\text{Im}\left(\frac{1}{\epsilon^* + 1}\right) = \frac{\epsilon_2}{(\epsilon_1 + 1)^2 + \epsilon_2^2} \tag{15}$$

The results are illustrated in Fig. 13 which shows that both VELF and SELF follow the same behavior with the incident photon energy. Additionally, energy loss due to free charge carriers travelling through the bulk material (VELF) is greater than energy loss due to free charge carriers traversing through the surface at certain peaks that define the C6 thin film (SELF). The real  $\sigma_1$  and imaginary  $\sigma_2$  parts of the optical conductivity can be determined using the  $\epsilon_1$  and  $\epsilon_2$  parts of the dielectric constant as stated by following expressions<sup>28,54</sup>:

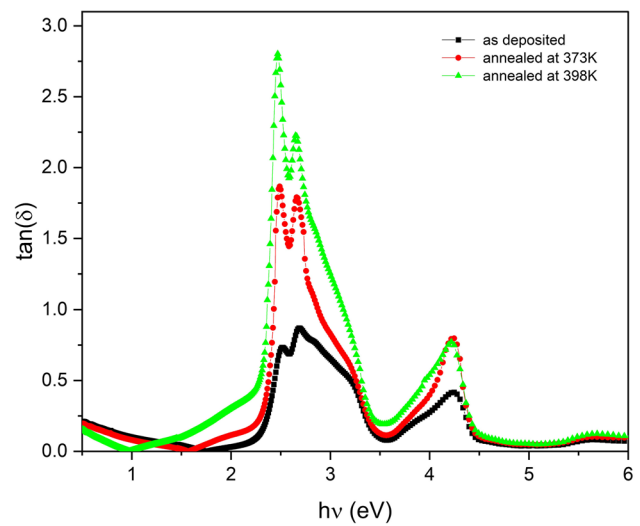


Fig. 12 The variation of  $\tan\delta$  with  $h\nu$  for as deposited and annealed thin films.

$$\sigma_1 = \omega\epsilon_0\epsilon_2 \text{ and } \sigma_2 = \omega\epsilon_0\epsilon_1 \tag{16}$$

The  $\sigma_1$  and  $\sigma_2$  parts of the optical conductivity of the investigated C6 thin film as a function of  $h\nu$  are illustrated in Fig. 14. The reduction in optical conductivity of C6 thin films  $\sigma_1$  and  $\sigma_2$  as annealing temperatures rise might be due to changes in crystallinity and charge carrier concentration. The variation in optical conductivity follows the same pattern as the change in dielectric constant.

### Nonlinearity in C6 Thin Films

Nonlinear optical materials exhibit fascinating properties such as second harmonic generation, sum and difference frequency generation, optical parameter amplification, and wave mixing and can be used in a wide variety of applications including optical computing, image manipulation and processing, data storage, and parametric oscillators.<sup>55</sup> The Wemple-DiDomenico (WDD) parameters ( $E_o$  and  $E_d$ ) are related to the nonlinear optical susceptibility,  $\chi^{(3)}$  through the following relationship<sup>45,54,56</sup>:

$$\chi^{(3)} = A[\chi^{(1)}]^4 = A \left[ \frac{E_o E_d}{4\pi(E_o^2 - (h\nu)^2)} \right]^4 \tag{17}$$

where  $A = 1.7 \times 10^{-10}$  (for  $\chi^{(3)}$  measured in esu) and has the same value for all materials that is assumed to be frequency independent, for  $h\nu \rightarrow 0$  one can obtain:

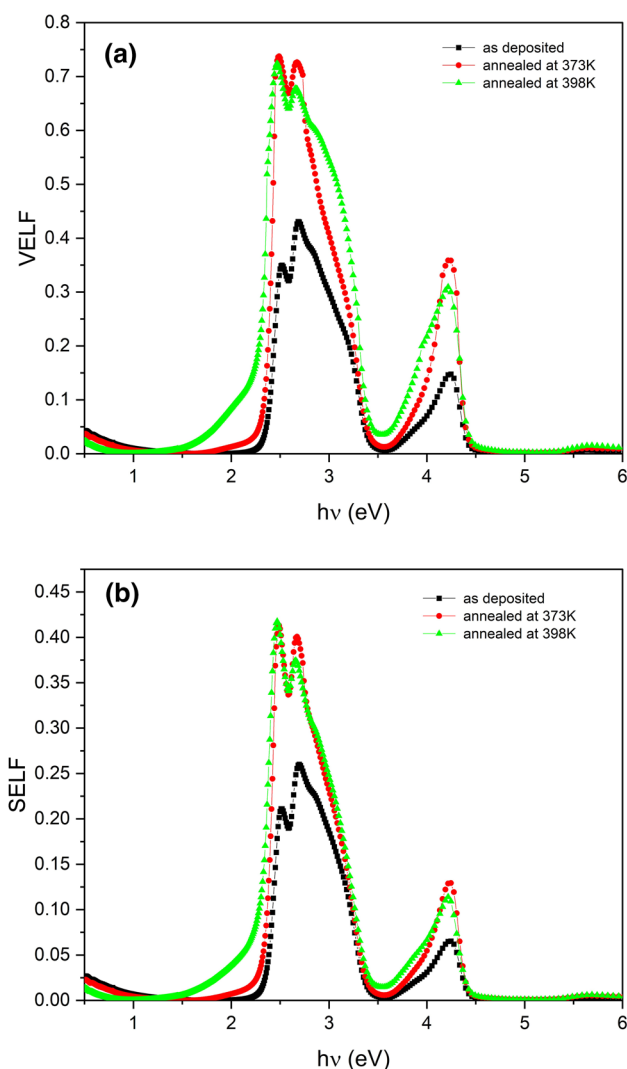


**Fig. 13** The variation of (a) VELF and (b) SELF with  $h\nu$  for as-deposited and annealed thin films.

$$\chi^{(3)} = 1.7 \left[ \frac{n_o^2 - 1}{4\pi} \right]^4 = 1.7 \left[ \frac{E_d}{4\pi E_o} \right]^4 \times 10^{-10} \quad (18)$$

The nonlinear refractive index  $n_2$  can be calculated by the following relation<sup>45</sup>:

$$n_{(2)} = \frac{12\pi \chi^{(3)}}{n_o} \quad (19)$$

The estimated values of nonlinear refractive index  $n_{(2)}$  and  $\chi^{(3)}$  (esu) when  $h\nu \rightarrow 0$  for the investigated films are listed in Table IV. The decreases in values of  $n_{(2)}$  and  $\chi^{(3)}$  as the annealing temperature increased was attributed to the decrease in  $E_g$  as the annealing temperature increased. This demonstrates that the nonlinear optical characteristics of C6 are very temperature sensitive.

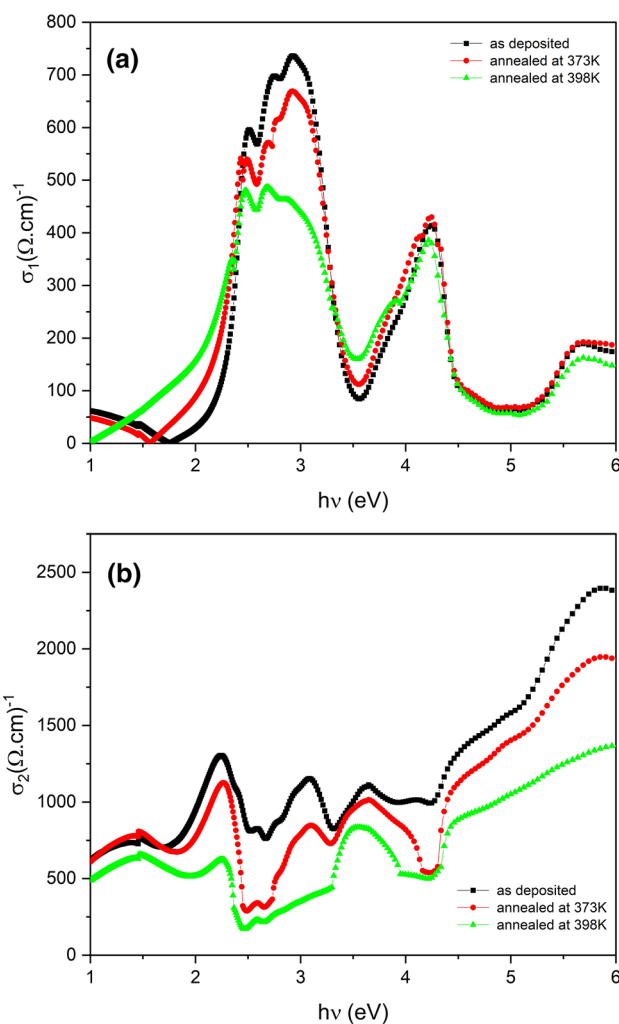


**Fig. 14** The variation of (a)  $\sigma_1$  and (b)  $\sigma_2$  for as-deposited and annealed thin films as a function of  $h\nu$ .

### Conclusions

In this study, the structural, morphological, and optical characteristics of C6 thin films were significantly impacted by the thermal annealing. An increase in crystallite size with annealing temperature was seen in the XRD patterns. The crystallite size values are in the nanometer range, indicating that the as-deposited and annealed films have nanostructure characteristics. The fact that the molecular structure of C6 films does not change as the annealing temperature goes up is proof that they are chemically stable. The indirect energy band gaps of corresponded to the Q, B, and N bands. The redshift in the indirect band gap for C6 films is observed due to the improved crystallinity of the thin film with higher annealing temperatures. Dispersion parameters ( $E_o, E_d, n_o$  and  $\epsilon_\infty$ ), dielectric parameters ( $N/m^*, \epsilon_L, \omega_p$ ), optical conductivity constants, and the loss energy functions (VELF and SELF) are correlated to the annealing temperatures.

The calculated  $\chi^{(3)}$  and  $n_{(2)}$  are on the order of  $\sim 10^{-13}$  and  $\sim 10^{-12}$  esu, respectively at  $h\nu \rightarrow 0$ . Lastly, these findings should be considered for linear and nonlinear optical properties recommend that the C6 film is good candidate for NLO applications in photonic and optoelectronic devices.

**Funding** Open access funding provided by The Science, Technology & Innovation Funding Authority (STDF) in cooperation with The Egyptian Knowledge Bank (EKB). This research did not receive any specific grant from funding agencies in the public, commercial, or not-for-profit sectors.

**Conflict of interest** the authors declare that there is no conflict of interest regarding the publication of this article.

**Data Availability** This manuscript has associated data in a data repository. [Authors' comment: All data included in this manuscript are available upon request by contacting the corresponding author.]

**Open Access** This article is licensed under a Creative Commons Attribution 4.0 International License, which permits use, sharing, adaptation, distribution and reproduction in any medium or format, as long as you give appropriate credit to the original author(s) and the source, provide a link to the Creative Commons licence, and indicate if changes were made. The images or other third party material in this article are included in the article's Creative Commons licence, unless indicated otherwise in a credit line to the material. If material is not included in the article's Creative Commons licence and your intended use is not permitted by statutory regulation or exceeds the permitted use, you will need to obtain permission directly from the copyright holder. To view a copy of this licence, visit <http://creativecommons.org/licenses/by/4.0/>.

## References

1. K.-L. Chen, H.-T. Liu, J.-H. Yu, Y.-H. Tung, Y.-S. Chou, C.-C. Yang, J.-S. Wang, J.-L. Shen, and K.-C. Chiu, Characterization of Coumarin-6 Polycrystalline Films Growth From Vacuum Deposition at Various Substrate Temperatures. *Sci. Rep.* 8, 16740 (2018).
2. A.A. Abuelwafa, M. Dongol, M.M. El-Nahass, and T. Soga, Role of Platinum Octaethylporphyrin (PtOEP) in PCPDTBT: PCBM Solar Cell Performance. *J. Mol. Struct.* 1202, 127303 (2020).
3. M. Tahir, Muddusir, D.N. Khan, S. Gul, F. Wahab, and S.M. Said, Photovoltaic Effect on the Microelectronic Properties of perylene/p-Si Heterojunction Devices, *J. Mater. Sci. Mater. Electron.* 30, 19463 (2019).
4. H. Kleemann, K. Krechan, A. Fischer, and K. Leo, A Review of Vertical Organic Transistors. *Adv. Funct. Mater.* 30, 1907113 (2020).
5. Y. Jiang, Y.-Y. Liu, X. Liu, H. Lin, K. Gao, W.-Y. Lai, and W. Huang, Organic Solid-State Lasers: A Materials View and Future Development. *Chem. Soc. Rev.* 49, 5885 (2020).
6. F.A. Mir, S. u Rehman, K. Asokan, S.H. Khan, and G.M. Bhat, Optical, DC and AC Electrical Investigations of 4-hydroxy Coumarin Molecule as an Organic Schottky Diode, *J. Mater. Sci. Mater. Electron.* 25, 1258 (2014).
7. Z.-S. Wang, K. Hara, Y. Dan-oh, C. Kasada, A. Shinpo, S. Suga, H. Arakawa, and H. Sugihara, Photophysical and (Photo)electrochemical Properties of a Coumarin Dye. *J. Phys. Chem. B.* 109, 3907 (2005).
8. X. Liu, J.M. Cole, P.G. Waddell, T.-C. Lin, J. Radia, and A. Zeidler, Molecular Origins of Optoelectronic Properties in Coumarin Dyes: Toward Designer Solar Cell and Laser Applications. *J. Phys. Chem. A.* 116, 727 (2012).
9. M. Edetsberger, M. Knapp, E. Gaubitzer, C. Miksch, K.E. Gvichiya, and G. Köhler, Effective Staining of Tumor Cells by Coumarin-6 Depends on the Stoichiometry of Cyclodextrin Complex Formation. *J. Incl. Phenom. Macrocycl. Chem.* 70, 327 (2011).
10. P.H. Lakner, M.G. Monaghan, Y. Möller, M.A. Olayioye, and K. Schenke-Layland, Applying Phasor Approach Analysis of Multiphoton FLIM Measurements to Probe the Metabolic Activity of Three-Dimensional In vitro Cell Culture Models. *Sci. Rep.* 7, 42730 (2017).
11. R.J. Nedumpara, T.K. J., J. V. K., C.P. Girijavallabhan, V.P.N. Nampoore, P. Radhakrishnan, Study of Solvent Effect in Laser Emission from Coumarin 540 Dye Solution, *Appl. Opt.* 46, 4786 (2007).
12. U.S. Raikar, C.G. Renuka, Y. Nadaf, B.G. Mulimani, A.M. Karguppikar, and M.K. Soudagar, Solvent Effects on the Absorption and Fluorescence Spectra of Coumarins 6 and 7 Molecules: Determination of Ground and Excited State Dipole Moment, *Spectrochim. Acta Part A Mol. Biomol. Spectrosc.* 65, 673 (2006).
13. J.-A. Cheng, C.-P. Chang, C.-H. Chen, and M.-S. Lin, The Fluorescent Quantum Efficiency of Copolymers Containing Coumarin-6 at the Side-chain. *J. Polym. Res.* 12, 53 (2005).
14. A. Uddin, C.B. Lee, and J. Wong, Emission Properties of Dopants Rubrene and Coumarin 6 in Alq<sub>3</sub> Films. *J. Lumin.* 131, 1037 (2011).
15. T.R. Hebner, C.C. Wu, D. Marcy, M.H. Lu, and J.C. Sturm, Ink-jet Printing of Doped Polymers for Organic Light Emitting Devices. *Appl. Phys. Lett.* 72, 519 (1998).
16. C.-C. Wu, J.C. Sturm, R.A. Register, J. Tian, E.P. Dana, and M.E. Thompson, Efficient Organic Electroluminescent Devices Using Single-Layer Doped Polymer Thin Films with Bipolar Carrier Transport Abilities. *IEEE Trans. Electron Devices.* 44, 1269 (1997).
17. Y.A.M. Ismail, T. Soga, and T. Jimbo, Photovoltaic Properties of Bulk Heterojunction Organic Solar Cell Composed of Coumarin 6 Dye as Light Harvester and Donor Material. *JJAP* 49, 052301 (2010).
18. Y.A.M. Ismail, T. Soga, and T. Jimbo, The Contribution of Coumarin 6 in Light Harvesting and Photocurrent of P3HT:PCBM Bulk Heterojunction Solar Cell. *Sol. Energy Mater. Sol. Cells* 94, 1406 (2010).
19. P. Kittichachachan, W. Soonpanich, and B. Damrongsak, Improved Light Harvesting in N719 Sensitized Nanocrystalline TiO<sub>2</sub> Solar Cells with Coumarin 6 Dye. *Energy Procedia.* 56, 152 (2014).
20. M. Saad Ebied, M. Dongol, M. Ibrahim, M. Nassary, S. Elnobi, and A.A. Abuelwafa, Effect of Carboxylic acid and Cyanoacrylic Acid as Anchoring Groups on Coumarin 6 Dye for Dye-Sensitized Solar Cells: DFT and TD-DFT Study. *Struct. Chem.* (2022). <https://doi.org/10.1007/s11224-022-01957-5>.
21. M. Dongol, M.M. El-Nahass, A. El-Denglawey, A.F. Elhady, and A.A. Abuelwafa, Optical Properties of Nano 5, 10, 15, 20-Tetraphenyl-21H, 23H-Prophyrin Nickel (II) Thin Films. *Curr. Appl. Phys.* 12, 1178 (2012).
22. A.A. Abuelwafa, M.S. Abd El-sadek, S. Elnobi, and T. Soga, Effect of Transparent Conducting Substrates on the Structure and Optical Properties of Tin (II) Oxide (SnO) Thin Films: Comparative Study. *Ceram. Int.* 47, 13510 (2021).
23. R.M. Matiur, A.A. Abuelwafa, S. Kato, N. Kishi, and T. Soga, A Comparative Study on Optical Properties of BiOI, Bi<sub>7</sub>O<sub>9</sub>I<sub>3</sub> and Bi<sub>5</sub>O<sub>7</sub>I Materials. *Opt. Mater.* 111, 110677 (2021).

24. J.P. Jasinski and E.S. Paight, 3-(2-Benzothiazolyl)-7-(diethylamino)coumarin, *Acta Crystallogr. Sect. C Cryst. Struct. Commun.* 51, 531 (1995).
25. X. Li and Y.-A. Son, C-H... $\pi$  and C-H...O Interactions in Coumarin 6: 3-(2-benzothiazolyl)-7-(diethylamino)-Coumarin Text. *Color. Finish.* 22, 83 (2010).
26. Y. Kijima and T. Hanada, Effect of the Pressure of Sputtering Atmosphere on the Physical Properties of Amorphous Aluminum Oxide Films. *J. Mater. Sci.* 35, 2193 (2000).
27. M. Dongol, A. El-Denglawey, A.F. Elhady, and A.A. Abuelwafa, Structural Properties of Nano 5, 10, 15, 20-Tetraphenyl-21H,23H-porphine Nickel (II) Thin Films. *Curr. Appl. Phys.* 12, 1334 (2012).
28. A.A. Abuelwafa, M.S. Abd El-sadek, and I.S. Yahia, Linear and Nonlinear Optical Properties of Nano-Spherical Perylenetetracarboxylic Dianhydride/ITO as a New Optical System. *Optic Laser Technol* 108, 241 (2018).
29. G.K. Williamson and R.E. Smallman, III Dislocation Densities in Some Annealed and Cold-Worked Metals from Measurements on the X-ray Debye-Scherrer Spectrum. *Philos. Mag.* 1, 34 (1956).
30. A.A. Abuelwafa, R. Md Matiur, A.A. Putri, and T. Soga, Synthesis, Structure, and Optical Properties of the Nanocrystalline Bismuth Oxyiodide (BiOI) for Optoelectronic Application. *Opt. Mater.* 109, 110413 (2020).
31. C.V. Ramana, R.J. Smith, and O.M. Hussain, Grain Size Effects on the Optical Characteristics of Pulsed-Laser Deposited Vanadium Oxide Thin Films. *Phys. Status Solidi Appl. Res.* 199, R4–R6 (2003).
32. A. Abdolazadeh Ziabari and F.E. Ghodsi, Growth, Characterization and Studying of Sol–Gel Derived CdS Nanocrystalline Thin Films Incorporated in Polyethyleneglycol: Effects of Post-heat Treatment. *Sol. Energy Mater. Sol. Cells.* 105, 249 (2012).
33. H.M. Alsoghier, M.A. Selim, H.M.A. Salman, H.M. Rageh, M.A. Santos, S.A. Ibrahim, M. Dongol, T. Soga, and A.A. Abuelwafa, NMR Spectroscopic, Linear and Non-linear Optical Properties of 1, 3-benzothiazol-2-yl-(phenylhydrazono) Acetonitrile (BTPA) Azo Dye. *J. Mol. Struct.* 1179, 315 (2019).
34. J. Tauc and A. Mentsh, States in the Gap. *Non Cryst. Solids* 8, 569 (1972).
35. R.M. Meixner, H. Göbel, F.A. Yildirim, W. Bauhofer, and W. Krautschneider, Wavelength-Selective Organic Field-Effect Phototransistors Based on Dye-Doped Poly-3-hexylthiophene. *Appl. Phys. Lett.* 89, 092110 (2006).
36. F.A. Akgul, G. Akgul, N. Yildirim, H.E. Unalan, and R. Turan, Influence of Thermal Annealing on Microstructural, Morphological, Optical Properties and Surface Electronic Structure of Copper Oxide Thin Films. *Mater. Chem. Phys.* 147, 987 (2014).
37. A.A. Abuelwafa, A. El-Denglawey, M. Dongol, M.M. El-Nahass, and T. Soga, Influence of Annealing Temperature on Structural and Optical Properties of Nanocrystalline Platinum Octaethylporphyrin (PtOEP) Thin Films. *Opt. Mater.* 49, 271 (2015).
38. M.M. El-Nahass, A.H. Ammar, A.A.M. Farag, A.A. Atta, and E.F.M. El-Zaidia, Effect of Heat Treatment on Morphological, Structural and Optical Properties of CoMTPP Thin Films. *Solid State Sci.* 13, 596 (2011).
39. M.M. El-Nahass, A.F. El-Deeb, H.S. Metwally, and A.M. Hasanien, Influence of Annealing on the Optical Properties of 5,10,15,20-tetraphenyl-21H, 23H-porphine Iron (III) Chloride Thin Films. *Mater. Chem. Phys.* 125, 247 (2011).
40. A.A. Abuelwafa, S. Elnobi, I. Yamada, N. Shibata, and T. Soga, Studying Linear and Nonlinear Optical Properties of Trifluoroethoxy-Coated Zinc Phthalocyanine ((TFEO) 4-ZnPc) Thin Films. *Opt. Mater.* 123, 111850 (2022).
41. M.M. El-Nahass, M. Emam-Ismaail, and M. El-Hagary, Structural, Optical and Dispersion Energy Parameters of Nickel Oxide Nanocrystalline Thin Films Prepared by Electron Beam Deposition Technique. *J. Alloys Compd.* 646, 937 (2015).
42. M.M. Shehata, H. Kamal, H.M. Hasheme, M.M. El-Nahass, and K. Abdelhady, Optical Spectroscopy Characterization of Zinc Tetra Pyridel Porphine (ZnTPyP) Organic Thin Films. *Opt. Laser Technol.* 106, 136 (2018).
43. M.M. El-Nahass, A.A.M. Farag, M. El-Metwally, F.S.H. Abu-Samaha, and E. Elesh, Structural, Absorption and Dispersion Characteristics of Nanocrystalline Copper Tetraphenyl Porphyrin Thin Films. *Synth. Met.* 195, 110 (2014).
44. H.M. Zeyada, M.M. El-Nahass, I.S. Elashmawi, and A.A. Habashi, Annealing Temperatures Induced Optical Constant Variations of Methyl Violet 2B Thin Films Manufactured by the Spin Coating Technique. *J. Non Cryst. Solids.* 358, 625 (2012).
45. S.H. Wemple and M. DiDomenico, Behavior of the Electronic Dielectric Constant in Covalent and Ionic Materials. *Phys. Rev. B.* 3, 1338 (1971).
46. M. Dongol, A.F. Elhady, M.S. Ebied, and A.A. Abuelwafa, Effect of Thermal Annealing on the Optical Properties of Ge<sub>20</sub>Se<sub>65</sub>S<sub>15</sub> Thin Films. *Indian J Phys.* 95, 1245 (2021).
47. HS Wasly, Abd El-Sadek, S.Elnobi, and A.A. Abuelwafa, Morphological, Structural, and Optical Properties of Flexible Tin Oxide (II) Thin Film Via Thermal Evaporation Technique, *Eur. Phys. J. Plus,* 137, 164 (2022)
48. M.S. AlKhalifah, I.M. El Radaf, and M.S. El-Bana, New Window Layer of Cu<sub>2</sub>CdSn<sub>3</sub>S<sub>8</sub> for Thin Film Solar Cells. *J. Alloys Compd.* 813, 152169 (2020).
49. H. Abdel-Khalek, M.I. El-Samahi, and A.M. El-Mahalawy, Plasma Impact on Structural, Morphological and Optical Properties of Copper Acetylacetonate Thin Films. *Spectrochim. Acta Mol. Biomol. Spectrosc.* 199, 356 (2018).
50. C.-M. Mo, L. Zhang, and G. Wang, Characteristics of Dielectric Behavior in Nanostructured Materials. *Nanostruct. Mater.* 6, 823 (1995).
51. H. Abdel-Khalek, E. Shalaan, M. Abd-El Salam, A.M. El-Sagheer, and A.M. El-Mahalawy, Effect of Thermal Annealing on Structural, Linear and Nonlinear Optical Properties of 1, 4, 5, 8-Naphthalene Tetracarboxylic Dianhydride Thin Films. *J. Mole. Struct.* 1178, 408 (2019).
52. H. Abd El-Khalek, M. Abd-El Salam, and F.M. Amin, Effect of Thermal Annealing and Aging Time on Optical Properties of Alphasexithiophene Thin Films. *Optical Mater.* 95, 109234 (2019).
53. S. Hunpratub, P. Thongbai, T. Yamwong, R. Yimnirun, and S. Maensiri, Dielectric Relaxations and Dielectric Response in Multiferroic BiFeO<sub>3</sub> Ceramics. *Appl. Phys. Lett.* 94, 062904 (2009).
54. A.A. Abuelwafa, A. El-Denglawey, M. Dongol, M.M. El-Nahass, and T. Soga, Structural and Optical Properties of Nanocrystalline Platinum octaethylporphyrin (PtOEP) Thin Films. *J. Alloys Compd.* 655, 415 (2016).
55. R.W. Boyd, G.L. Fischer, in: *Nonlinear Optical Materials*, Encyclopedia of Materials: Science and Technology, (Elsevier, 2001), pp. 6237–6244
56. H. Tichá and L. Tichý, Semiempirical Relation Between Non-linear Susceptibility (Refractive Index), Linear Refractive Index and Optical Gap and its Application to Amorphous Chalcogenides. *J. Optoelectron. Adv. Mater.* 4, 381 (2002).

**Publisher's Note** Springer Nature remains neutral with regard to jurisdictional claims in published maps and institutional affiliations.

## Authors and Affiliations

Mostafa Saad Ebied<sup>1</sup> · Mahmoud Dongol<sup>1</sup> · Medhat Ibrahim<sup>2,3</sup> · Mohammed Nassary<sup>4</sup> · Sahar Elnobi<sup>4</sup> · Amr Attia Abuelwafa<sup>1</sup> 

✉ Amr Attia Abuelwafa  
a.a.abuelwafa@gmail.com

<sup>1</sup> Nano and Thin film Lab. Physics Department, Faculty of Science, South Valley University, Qena 83523, Egypt

<sup>2</sup> Molecular Spectroscopy and Modeling Unit, Spectroscopy Department, National Research Centre, 33 El-Bohouth Str, Dokki, Giza 12622, Egypt

<sup>3</sup> Nanotechnology Research Centre (NTRC), The British University in Egypt (BUE), Suez Desert Road, El-Sherouk City, Cairo 11837, Egypt

<sup>4</sup> Physics Department, Faculty of Science, South Valley University, Qena 83523, Egypt